ЖЭТФ, 2015, том 148, вып. 3 (9), стр. 584–596

SURFACE STATES IN A 3D TOPOLOGICAL INSULATOR: THE ROLE OF HEXAGONAL WARPING AND CURVATURE

E. V. Repin [a] **, *I. S. Burmistrov*** [a,b*]

[a] *Moscow Institute of Physics and Technology*
141700, Moscow, Russia

[b] *L. D. Landau Institute for Theoretical Physics Russian Academy of Sciences*
119334, Moscow, Russia

Received June 3, 2015

We explore a combined effect of hexagonal warping and a finite effective mass on both the tunneling density of electronic surface states and the structure of Landau levels of 3D topological insulators. We find the increasing warping to transform the square-root van Hove singularity into a logarithmic one. For moderate warping, an additional logarithmic singularity and a jump in the tunneling density of surface states appear. By combining the perturbation theory and the WKB approximation, we calculate the Landau levels in the presence of hexagonal warping. We predict that due to the degeneracy removal, the evolution of Landau levels in the magnetic field is drastically modified.

DOI: 10.7868/S0044451015090151

1. INTRODUCTION

Theoretical and experimental study of three dimensional (3D) topological insulators is in the focus of modern research in condensed matter physics [1–3]. Apart from fundamental interest in the novel quantum state of matter — topological insulators — attract great attention in view of their possible applications in spintronics due to spin-current locking of surface states. Many exciting features of electron states on the surface of a 3D topological insulator were found within the simplest two-dimensional (2D) Hamiltonian, linear in momentum and spin operators, that is allowed by the time-reversal and crystal symmetries [1–3].

Recently, it was realized that without symmetry violation, this simplest Hamiltonian can be extended to higher-order terms in momentum describing finite-mass and hexagonal warping of surface states [4, 5]. Indeed, the hexagonal warping of their Fermi surface has been found experimentally by angle-resolved photoemission spectroscopy in topological insulators such as Bi_2Te_3 [6, 7], Bi_2Se_3 [8], and $Pb(Bi,Sb)_2Te_4$ [9]. Theoretically, the hexagonal warping of surface states can induce spin-density wave instability [4], affects the dc and optical conductivities [10, 11], is responsible for localization of the Cherenkov sound in certain directions [12], and can stabilize the $\nu = 1/3$ fractional quantum Hall state [13]. In addition to the hexagonal warping, spin and angle resolved photoemission spectroscopy revealed the presence of finite curvature of the spectrum of surface states in Bi_2Te_3, Bi_2Se_3, $Pb(Bi,Sb)_2Te_4$, and $TlBiSe_2$ [9].

An alternative experimental way to access the spectrum of surface states in 3D topological insulators is the scanning tunneling microscopy. Recently, scanning tunneling microscopy was employed for Bi_2Te_3 [7, 14–17], Bi_2Se_3 [14, 18–22], and Sb_2Te_3 in a perpendicular magnetic field [21]. The spectrum of surface states extracted from angle-resolved photoemission spectroscopy data is correlated with the tunneling conductance measured by scanning tunneling microscopy [7]. However, bulk states also contribute to the tunneling conductance, thus hiding a part due to the surface states. To unravel the surface contribution, it is crucial to know the tunneling density of surface states (TDOSS) in detail. Within the spectrum linear in momentum, the TDOSS with and without the magnetic field was studied theoretically in Refs. [23–25]. In spite of clear experimental relevance, we are not aware of theoretical studies of the TDOSS in the presence of nonzero curvature and hexagonal warping.

*E-mail: burmi@itp.ac.ru

In this paper, we calculate the tunneling density of states on the surface of a 3D topological insulator in the presence of hexagonal warping and a finite mass m. We demonstrate that hexagonal warping leads to a logarithmic van Hove singularity instead of the square-root one that exists in the case of a finite mass due to the end point of the spectrum. For moderate values of the hexagonal warping, we discover an additional logarithmic singularity and a jump in the TDOSS. This prediction is quantitatively supported by scanning tunneling microscopy measurements of the local density of states in Bi_2Te_3. In the presence of a perpendicular magnetic field, we analyze the structure of Landau levels within the perturbation theory and in the WKB approximation. As is well known [26], in the absence of hexagonal warping, there are crossings of Landau levels at some magnetic fields due to a finite mass. We find that the hexagonal warping removes these degeneracies and strongly affects the slope of Landau levels with respect to the magnetic field.

The paper is organized as follows. In Sec. 2, we introduce the model Hamiltonian and calculate the tunneling density of states on the surface of a 3D topological insulator in the presence of hexagonal warping and finite mass. In Sec. 3, we analyze the effect of hexagonal warping on Landau levels within the perturbation theory. In Sec. 4, we investigate the structure of Landau levels in the presence of hexagonal warping in the WKB approximation. We conclude with a discussion of how our theoretical results can be further tested experimentally (Sec. 5).

2. TUNNELING DENSITY OF SURFACE STATES AT ZERO MAGNETIC FIELD

We start from the model Hamiltonian of electron states on the surface of a 3D topological insulator in zero magnetic field, given by the 2×2 matrix [4, 5]

$$\mathcal{H} = v\big(k_x\sigma_y - k_y\sigma_x\big) + \frac{k_x^2+k_y^2}{2m} + \frac{\lambda}{2}\big(k_+^3+k_-^3\big)\sigma_z. \qquad (1)$$

Here, $\mathbf{k} = \{k_x, k_y\}$ denotes the in-plane quasiparticle momentum, $k_\pm = k_x \pm ik_y$, and $\sigma_{x,y,z}$ are the Pauli matrices. We note that due to the spin–orbit coupling in the bulk, the Pauli matrices $\sigma_{x,y,z}$ do not necessarily correspond to operators of the electron spin [27, 28]. The first term in the right-hand side of Eq. (1) describes the conical (Dirac-type) spectrum with a velocity v. The second term in Eq. (1) takes a finite curvature of the surface state spectrum into account. The effective mass m can be positive (e. g., for Bi_2Se_3) or negative (as in the case of Bi_2Te_3) [9]. In what follows, having in mind the case of Bi_2Te_3, we consider the situation where $m < 0$. The results for the opposite case, $m > 0$, can be easily obtained by inversion of the energy and momentum. The last term in Eq. (1) describes the effect of hexagonal warping, whose strength is characterized by the parameter λ. In the absence of hexagonal warping, $\lambda = 0$, Hamiltonian (1) is just the Bychkov–Rashba Hamiltonian for 2D electrons with spin–orbit splitting [26]. To Hamiltonian (1), we can add a term of the third order in the momentum describing the $\mathbf{k}^2$ contribution to the velocity v [4]. Moreover, in extending Hamiltonian (1) to the fifth order in k, Dresselhaus spin–orbit terms were proposed to explain deviation of the electron spin from the direction perpendicular to the momentum [29]. However, recent results of spin and angle resolved photoemission spectroscopy [9] do not demonstrate significant deviation of the surface state spectrum from the one corresponding to Eq. (1). Therefore, we confine our considerations to Hamiltonian (1).

The spectrum of Hamiltonian (1) has the form [4, 5]

$$E_\pm(k,\theta) = \frac{k^2}{2m} \pm \sqrt{v^2k^2 + \lambda^2k^6\cos^2 3\theta}, \qquad (2)$$

where θ parameterizes the momentum, and

$$k_x = k\cos\theta, \quad k_y = k\sin\theta.$$

The TDOSS can be written as

$$g(E) = \sum_{s=\pm}\int\limits_0^\infty \frac{kdk}{(2\pi)^2}\int\limits_0^{2\pi} d\theta\,\delta\big(E - E_s(k,\theta)\big). \qquad (3)$$

It is convenient to introduce the energy parameters

$$E_0 = \sqrt{v^3/\lambda}, \quad \Delta = 2|m|v^2$$

to characterize the hexagonal warping and curvature, respectively. Then the dimensionless parameter

$$\alpha = (\Delta/E_0)^4$$

measures the strength of hexagonal warping in comparison with curvature. We remind that in the absence of warping, $\alpha = \lambda = 0$, the density of states is given by

$$g_{\lambda=0}(E) = \frac{\Delta}{2\pi v^2} \times \begin{cases} 1, & E < 0, \\ (1-4E/\Delta)^{-1/2}, & 0 \leqslant E < \Delta/4, \\ 0, & \Delta/4 < E. \end{cases} \qquad (4)$$

It has a square-root van Hove singularity at $E = \Delta/4$, which is the end point of the spectrum. For nonzero hexagonal warping, $\alpha > 0$, the TDOSS is

$$g(E) = \frac{\Delta}{2\pi v^2} F(E/\Delta, \alpha), \tag{5}$$

where

$$F(\epsilon,\alpha) = \frac{1}{\pi}\int\limits_0^\infty dx\,|\epsilon + x|\,\mathrm{Re}\,\frac{1}{\sqrt{(\epsilon+x)^2 - x}} \times \\ \times\,\mathrm{Re}\,\frac{1}{\sqrt{\alpha x^3 + x - (\epsilon+x)^2}}. \tag{6}$$

The limits of integration over x in Eq. (6) are in fact determined by the regions where the radicands are positive. Depending on the values of ϵ and α, the cubic polynomial

$$y_3(x) = \alpha x^3 + x - (\epsilon + x)^2$$

can have one (see curves *A1*, *A2*, *A4*, and *A5* in Fig. 1*a*) or three (see curve *A3* in Fig. 1*a*) real roots. The regions of the corresponding behavior in the $\{\epsilon, \alpha\}$ plane are shown in Fig. 1*b*. There is region *A5* above the line $\epsilon = 1/2$. Region *A1* is situated below the curve

$$\alpha_1(\epsilon) = \frac{1}{3(1-2\epsilon)}.$$

Region *A3* is clamped between the curves parameterized as $\alpha = \alpha_-(\epsilon)$ and $\alpha = \alpha_+(\epsilon)$, where

$$\alpha_\pm(\epsilon) = \frac{2(\epsilon + z_\pm(\epsilon)) - 1}{3z_\pm^2(\epsilon)}, \\ z_\pm(\epsilon) = 1 - 2\epsilon \pm \sqrt{(1-2\epsilon)^2 - 3\epsilon^2}. \tag{7}$$

The curves $\alpha = \alpha_\pm(\epsilon)$ merge and end at the points

$$\epsilon_c = 1/\left(2+\sqrt{3}\right) \approx 0.27, \quad \alpha_c = \left(3+2\sqrt{3}\right)/9 \approx 0.71.$$

Region *A2* is below region *A5* but above the curve parameterized as

$$\alpha = \max\{\alpha_-(\epsilon), \alpha_1(\epsilon)\}.$$

Region *A4* is clamped between the curves $\alpha = \alpha_+(\epsilon)$ and $\alpha = \alpha_1(\epsilon)$.

We let c_1, c_2, c_3 denote the roots of the cubic polynomial $y_3(x)$ in increasing order if there exist three real roots, and let c_i, where $i = 1$ or 3, be the root of $y_3(x)$ in the case of a single real root only. We note that z_- (z_+) coincides with c_1 and c_2 (c_2 and c_3) at the point where they merge. The roots of the quadratic polynomial

$$y_2(x) = (\epsilon + x)^2 - x$$

Table 1. Expressions for the function $F(\epsilon, \alpha)$ in different regions of the $\{\epsilon, \alpha\}$ plane

	$\epsilon < 1/4$	$\epsilon \geqslant 1/4$
A1	$F = F_1 + F_5$	$F = F_3 + F_4$
A2		$F = F_3$
A3	$F = F_1 + F_2 + F_3$	$F = F_3 + F_4$
A4	$F = F_1 + F_5$	$F = F_3 + F_4$
A5		$F = F_3$

are given as

$$x_{1,2} = \left(1 - 2\epsilon \mp \sqrt{1-4\epsilon}\,\right)/2.$$

It is convenient to introduce the following functions:

$$F_1 = \int\limits_{c_1}^{x_1} dx\,\mathcal{F}(x,\epsilon,\alpha), \quad F_2 = \int\limits_{x_2}^{c_2} dx\,\mathcal{F}(x,\epsilon,\alpha), \\ F_3 = \int\limits_{c_3}^{\infty} dx\,\mathcal{F}(x,\epsilon,\alpha), \quad F_4 = \int\limits_{c_1}^{c_2} dx\,\mathcal{F}(x,\epsilon,\alpha), \\ F_5 = \int\limits_{x_2}^{\infty} dx\,\mathcal{F}(x,\epsilon,\alpha), \tag{8}$$

where

$$\mathcal{F}(x,\epsilon,\alpha) = \frac{1}{\pi}\,\frac{|\epsilon + x|}{\sqrt{(\epsilon+x)^2 - x}\sqrt{\alpha x^3 + x - (\epsilon+x)^2}}. \tag{9}$$

Then for each region in Fig. 1*b*, the function $F(\epsilon, \alpha)$ can be represented as a linear combination of the functions F_i, $i = 1, \ldots, 5$, with coefficients equal to 0 or 1 (see Table 1).

The TDOSS exhibits singular behavior on the line $\epsilon = 1/4$ and on the curves $\alpha = \alpha_\pm(\epsilon)$. The logarithmic divergence at $\epsilon = 1/4$ for any $\alpha > 0$ supersedes the square-root singularity at the same energy existing in the case $\alpha = 0$. Formally, it is due to the confluence of two real roots $x_{1,2}$ of the quadratic polynomial $y_2(x)$. The asymptotic form of $F(\epsilon, \alpha)$ near this logarithmic singularity is

$$F(\epsilon,\alpha) \approx \frac{4}{\pi\sqrt{\alpha}} \ln\frac{1}{|\epsilon - 1/4|}, \quad |\epsilon - 1/4| \ll 1. \tag{10}$$

There is an other logarithmic divergence of the density of states on the curve $\alpha = \alpha_+(\epsilon)$. Within the logarithmic accuracy, the asymptotic behavior of the function F near $\alpha = \alpha_+(\epsilon)$ can be found as

$$F(\epsilon,\alpha) \approx \frac{\Delta_+}{\pi} \ln\frac{1}{|\alpha - \alpha_+(\epsilon)|}, \quad |\alpha - \alpha_+(\epsilon)| \ll 1, \tag{11}$$

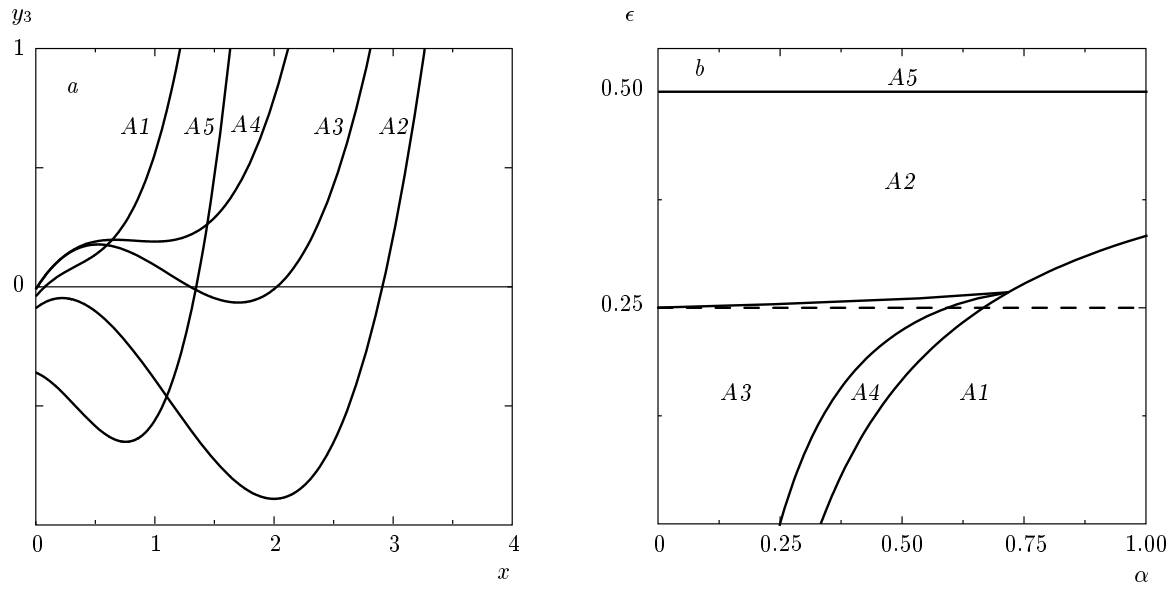

Fig. 1. The five different types of possible behavior of a cubic polynomial $y_3(x)$ (a). The five corresponding regions in the $\{\epsilon, \alpha\}$ plane (b)

where

$$\Delta_+ = \\ = \frac{|\epsilon + z_+(\epsilon)|}{[(\epsilon+z_+(\epsilon))^2 - z_+(\epsilon)]^{1/2}[1-3(1-2\epsilon)\alpha_+(\epsilon)]^{1/4}}. \quad (12)$$

At the border between regions $A2$ and $A3$, there is a jump of the density of states due to the appearance of an infinitely small range of integration between the first two roots c_1 and c_2 of the cubic polynomial $y_3(x)$. For the jump of the function $F(\epsilon, \alpha)$ at $\alpha = \alpha_-(\epsilon)$, we find

$$F(\epsilon, \alpha_- - 0) - F(\epsilon, \alpha_- + 0) = \lim_{c_1 \to c_2} \int_{c_1}^{c_2} \frac{dx}{\pi\sqrt{\alpha}} \times \\ \times \frac{|\epsilon + x|[(\epsilon + x)^2 - x]^{-1/2}}{[(c_3 - x)(x - c_1)(c_2 - x)]^{1/2}} = \Delta_-. \quad (13)$$

Here, Δ_- is given by Eq. (12) after the substitution of z_- and α_- for z_+ and α_+, respectively.

Therefore, for $\alpha > 0$, the square-root divergence of the density of states at $E = \Delta/4$ is split into a logarithmic divergence and a jump. The latter exists for $\alpha < \alpha_c$ only. The second logarithmic divergence appears from $\epsilon = -\infty$ as α increases from the zero value. Such a nontrivial behavior of the TDOSS (the function $F(\epsilon, \alpha)$) is illustrated in Fig. 2.

As usual, the van Hove singularities in the density of states discussed above can be explained by a complicated, not linearly connected shape of a Fermi surface

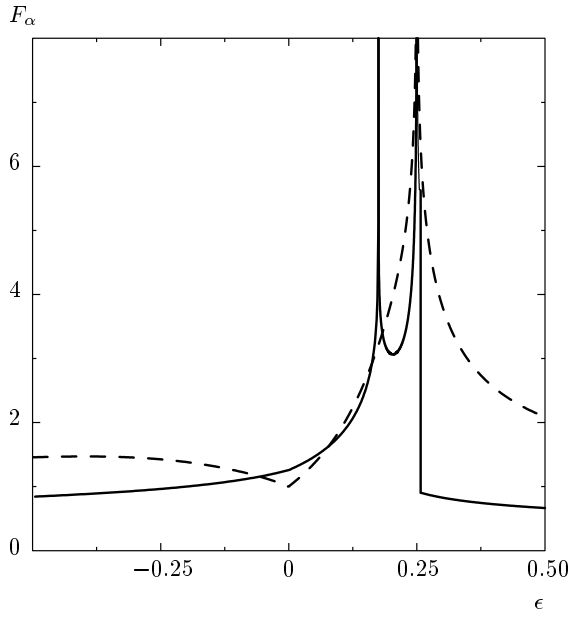

Fig. 2. The normalized TDOSS versus dimensionless energy $\epsilon = E/\Delta$ for $\alpha = 0.4$ (solid curve) and $\alpha = 22$ (dashed curve)

for the spectrum, Eq. (2). The Fermi surface is illustrated graphically in Fig. 3. Depending on the values of α, there are three different cases of possible evolution of the Fermi surface with an increase in the chemical potential (energy). In the case $\alpha > \alpha_c$, there is

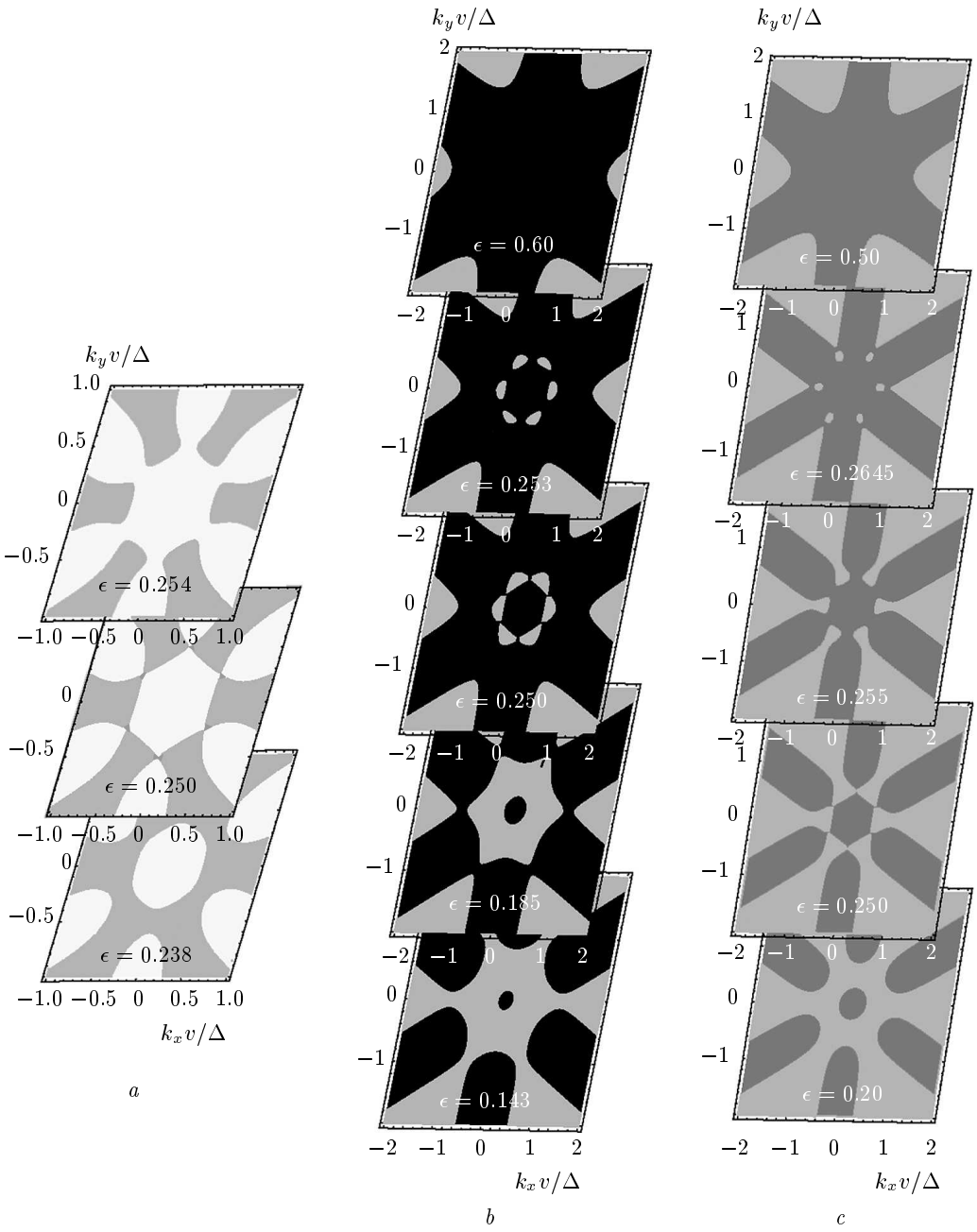

Fig. 3. The constant energy cuts of energy spectrum (2) for (a) $\alpha = 1$ and $\epsilon = 0.238, 0.25, 0.254$ from the bottom to the top, (b) $\alpha = 0.4$ and $\epsilon = 0.143, 0.185, 0.253, 0.6$, and ($c$) $\alpha = 0.68$ and $\epsilon = 0.2, 0.25, 0.255, 0.5$. Color online see arXiv:1408.6960

one logarithmic divergence of the density of states at $E = \Delta/4$. It occurs because the central snowflake-like part enclosing the $\bar{\Gamma}$ point touches the six outermost disconnected parts (see Fig. 3a, panel $\epsilon = 0.250$). For $\alpha < \alpha_0$, where

$$\alpha_0 = \alpha_+(1/4) = 16/27 \approx 0.59,$$

two logarithmic singularities exist in the density of states. The first one at $E = \epsilon_+\Delta$ (ϵ_+ is determined as the solution of the equation $\alpha = \alpha_+(\epsilon_+)$) is related to the six outermost disconnected parts touching each other (see Fig. 3b, panel $\epsilon = 0.185$). The second singularity situated at $E = \Delta/4$ is due to the touching of the central snowflake-like part and the part formed

after consolidation of six initially disconnected pieces (see Fig. 3*b*, panel $\epsilon = 0.250$). The jump in the density of states at $E = \epsilon_-\Delta$ (ϵ_- is determined as the solution of the equation $\alpha = \alpha_-(\epsilon_-)$) is related to disappearance of six empty spots (see Fig. 3*b*, panel $\epsilon = 0.255$). In the intermediate range $\alpha_0 < \alpha \leqslant \alpha_c$, there are two logarithmic singularities of the density of states. The first one at $E = \Delta/4$ is due to the central snowflake-like part touching the six outermost disconnected parts (see Fig. 3*c*, panel $\epsilon = 0.250$). The second singularity at $E = \epsilon_+\Delta$ is related to the appearance of six empty spots (see Fig. 3*c*, panel $\epsilon = 0.255$). The jump in the density of state is due to the collapse of these empty spots (see Fig. 3*c*, panel $\epsilon = 0.2645$).

3. LANDAU LEVELS WITHIN THE PERTURBATION THEORY

We now consider the effect of the magnetic field H perpendicular to the surface of a 3D topological insulator on the spectrum of surface states. In general, one needs to start from a Hamiltonian describing bulk states in the presence of the magnetic field and to derive the effective 2D Hamiltonian for the surface states from it. It was shown [30] that such an approach leads to the results that are similar to the results that can be obtained from the zero-field Hamiltonian for the surface states after the Peierls substitution. Therefore, to describe the surface states in a perpendicular magnetic field, we substitute the momentum $\mathbf{k}$ in Hamiltonian (1) with $\mathbf{k} - e\mathbf{A}$. Here, $\mathbf{A}$ denotes the vector potential for the perpendicular magnetic field $\mathbf{H} = \nabla \times \mathbf{A}$, and e stands for the electron charge. In addition, the Zeeman term $g_L\mu_B H\sigma_z/2$ (g_L and μ_B are the g-factor and Bohr magneton) has to be added to Hamiltonian (1). Here, we assume for simplicity the (111) surface such that $\boldsymbol{\sigma}/2$ coincides with the electron spin operator [27, 28]. Thus, we consider the following Hamiltonian

$$\mathcal{H} = \frac{(\mathbf{k} - e\mathbf{A})^2}{2m} + v\big[(\mathbf{k} - e\mathbf{A}), \boldsymbol{\sigma}\big]_z + \\ + \frac{\lambda}{2}\sum_{s=\pm}(k_s - eA_s)^3\sigma_z + \frac{1}{2}g_L\mu_B H\sigma_z, \quad (14)$$

where

$$A_\pm = A_x \pm iA_y.$$

In the case $\lambda = 0$, Hamiltonian (1) describes 2D electrons with a Rashba-type spin-orbit splitting in the presence of a magnetic field. [26]. Then the spectrum (Landau levels) are known to be as follows [26]:

$$E_n^s = -n\omega_c + s\sqrt{E_0^2 + \frac{2nv^2}{l_H^2}}, \quad n = 1, 2, \ldots, \quad s = \pm, \\ E_0 = -\frac{\omega_c}{2} - \frac{g_L\mu_B H}{2}. \quad (15)$$

Here,

$$l_H = \frac{1}{\sqrt{|e|H}}, \quad \omega_c = \frac{|e|H}{|m|}$$

are the magnetic length and the cyclotron frequency. The corresponding wave functions in the Landau gauge,

$$\mathbf{A} = (-Hy, 0, 0),$$

reads

$$\psi_{n,s} = \frac{e^{ik_x x}}{\sqrt{L_x}}\begin{pmatrix}\alpha_{n,s}|n-1\rangle \\ \alpha_{n,-s}|n\rangle\end{pmatrix}, \quad (16)$$

where L_x denotes the size of the surface in the x direction and $|n\rangle$ stands for standard states of the Landau level problem. The coefficients $\alpha_{n,s}$ can be written as

$$\alpha_{n,s} = \frac{1}{\sqrt{1 + D_n^2}}\begin{cases}-isD_n, & s\operatorname{sgn}E_0 > 0, \\ 1, & s\operatorname{sgn}E_0 < 0,\end{cases} \quad (17)$$

where

$$D_n = \frac{\sqrt{2n}v/l_H}{|E_0| + \sqrt{E_0^2 + 2nv^2/l_H^2}}. \quad (18)$$

To treat the hexagonal warping in Hamiltonian (14) as a perturbation, we need to evaluate matrix elements of the operator

$$V = \frac{\lambda}{2}\sum_{s=\pm}(k_s - eA_s)^3\sigma_z \equiv \frac{\sqrt{2}\lambda}{l_H^3}\big(\hat{a}^3 + \hat{a}^{\dagger 3}\big)\sigma_z. \quad (19)$$

Here, the boson operators $\hat{a}$ and $\hat{a}^\dagger$ are defined as

$$\hat{a} = \frac{l_H}{\sqrt{2}}\big(k_- - eA_-\big), \quad \hat{a}^\dagger = \frac{l_H}{\sqrt{2}}\big(k_+ - eA_+\big). \quad (20)$$

The state $|n\rangle$ is an eigenstate of the operator $\hat{a}^\dagger\hat{a}$, $\hat{a}^\dagger\hat{a}|n\rangle = n|n\rangle$. Using the well-known matrix elements of the operators $\hat{a}$ and $\hat{a}^\dagger$, we obtain the following results for the matrix elements:

$$V_{n,n+3}^{s,s'} = \frac{\sqrt{2}\lambda}{l_H^3} \times \\ \times \big(\overline{\alpha_{n,s}}\alpha_{n+3,s'}\zeta_{n+2} - \overline{\alpha_{n,-s}}\alpha_{n+3,-s'}\zeta_{n+3}\big), \quad (21)$$

where $s, s' = \pm$, the bar denotes complex conjugation, and

$$\zeta_n = \sqrt{n(n-1)(n-2)} \quad \text{for} \quad n \geqslant 0.$$

The other nonzero matrix elements can be obtained by complex conjugation. Hence, the second-order correction to eigenenergies (15) due to the hexagonal warping is given as

$$\delta E_n^{s,(2)} = -\sum_{s'=\pm} \left(\frac{|V_{n+3,n}^{s',s}|^2}{E_{n+3}^{s'} - E_n^s} + \frac{|V_{n-3,n}^{s',s}|^2}{E_{n-3}^{s'} - E_n^s} \right). \quad (22)$$

For small values of n (for low-lying Landau levels), the perturbation theory is applicable if

$$\lambda/l_H^3 \ll \max\{\omega_c, v/l_H\}.$$

The second-order correction $\delta E_n^{s,(2)}$ increases with an increase in n. Therefore, the perturbation theory breaks down at large n if λ is not sufficiently small. Setting

$$\mathcal{X} = \lambda/v l_H^2, \quad \mathcal{Y} = 2|m| l_H v,$$

we find that perturbative result (22) is valid if the following inequalities hold:

$$1 \gg \mathcal{X} n \begin{cases} \mathcal{Y}\sqrt{n}, & \mathcal{Y}\sqrt{n} \ll 1, \\ 1, & 1 \ll \mathcal{Y}\sqrt{n} \ll n, \\ \mathcal{Y}/\sqrt{n}, & n \ll \mathcal{Y}\sqrt{n}. \end{cases} \quad (23)$$

In addition the perturbation theory in (22) does not work near crossings of the unperturbed levels E_n^+ and E_{n+3}^+ that occur with varying the magnetic field. To improve the perturbation theory near these degeneracy points, we apply a unitary transformation of the Hamiltonian that diagonalizes the 2×2 matrix

$$A = \begin{pmatrix} E_n^+ & V_{n,n+3}^{++} \\ V_{n,n+3}^{++} & E_{n+3}^+ \end{pmatrix}. \quad (24)$$

As usual, the eigenvalues of the matrix A,

$$\Lambda_\pm = \frac{E_{n+3}^+ + E_n^+}{2} \pm \pm \frac{1}{2}\sqrt{(E_{n+3}^+ - E_n^+)^2 + 4|V_{n,n+3}^{++}|^2}, \quad (25)$$

describe the avoided crossing of levels E_n^+ and E_{n+3}^+ due to the matrix element $V_{n,n+3}^{++}$. For a given n, we start from rewriting Hamiltonian (1) in the basis of the unperturbed states $\psi_{n,s}$:

$$\mathcal{H} = \begin{pmatrix} A & B \\ B^\dagger & C \end{pmatrix}. \quad (26)$$

Here, we introduce the infinite-block matrices

$$B = \begin{pmatrix} V_{n,n+3}^{+-} & V_{n,n-3}^{++} & V_{n,n-3}^{+-} & 0 & 0 & 0 & \dots \\ 0 & 0 & 0 & V_{n+3,n}^{+-} & V_{n+3,n+6}^{++} & V_{n+3,n+6}^{+-} & \dots \end{pmatrix},$$

$$C = \begin{pmatrix} E_{n+3}^- & 0 & 0 & V_{n+3,n}^{--} & V_{n+3,n+6}^{-+} & V_{n+3,n+6}^{--} & \dots \\ 0 & E_{n-3}^+ & 0 & V_{n-3,n}^{+-} & 0 & 0 & \dots \\ 0 & 0 & E_{n-3}^- & V_{n-3,n}^{--} & 0 & 0 & \dots \\ V_{n,n+3}^{--} & V_{n,n-3}^{-+} & V_{n,n-3}^{--} & E_n^- & 0 & 0 & \dots \\ V_{n+6,n+3}^{+-} & 0 & 0 & 0 & E_{n+6}^+ & 0 & \dots \\ V_{n+6,n+3}^{--} & 0 & 0 & 0 & 0 & E_{n+6}^- & \dots \\ \dots & \dots & \dots & \dots & \dots & \dots & \dots \end{pmatrix}. \quad (27)$$

The unitary transformation diagonalizing the matrix A is as follows:

$$U = \begin{pmatrix} u & 0 \\ 0 & 1 \end{pmatrix}, \quad u = \begin{pmatrix} \dfrac{1}{\sqrt{1+\gamma_+^2}} & \dfrac{1}{\sqrt{1+\gamma_-^2}} \\ \dfrac{\gamma_+}{\sqrt{1+\gamma_+^2}} & \dfrac{\gamma_-}{\sqrt{1+\gamma_-^2}} \end{pmatrix}, \quad (28)$$

$$\gamma_{\pm} = \frac{E^{+}_{n+3} - E^{+}_{n} \pm \sqrt{(E^{+}_{n} - E^{+}_{n+3})^2 + 4|V^{+-}_{n,n+3}|^2}}{2V^{++}_{n,n+3}}. \quad (29)$$

Now taking into account the matrix elements (given by $u^{\dagger}B$) connecting levels $\Lambda_{\pm}$ with the other levels within the second-order perturbation theory, we find the following results for energies corresponding to the unperturbed energies E^{+}_{n} and E^{+}_{n+3}:

$$E_{\pm} = \Lambda_{\pm} + \frac{1}{1+\gamma_{\pm}^2}\left(\frac{|V^{+-}_{n,n+3}|^2}{\Lambda_{\pm} - E^{-}_{n+3}} + \frac{|V^{++}_{n,n-3}|^2}{\Lambda_{\pm} - E^{+}_{n-3}} + \right.$$
$$+ \frac{|V^{+-}_{n,n-3}|^2}{\Lambda_{\pm} - E^{-}_{n-3}} + \frac{|\gamma_{\pm} V^{+-}_{n+3,n}|^2}{\Lambda_{\pm} - E^{-}_{n}} +$$
$$\left. + \frac{|\gamma_{\pm} V^{++}_{n+3,n+6}|^2}{\Lambda_{\pm} - E^{+}_{n+6}} + \frac{|\gamma_{\pm} V^{+-}_{n+3,n+6}|^2}{\Lambda_{\pm} - E^{-}_{n+6}} \right). \quad (30)$$

This result is free from the fictitious divergence at the point $E^{+}_{n} = E^{+}_{n+3}$ produced within the standard perturbation theory, Eq. (22). Away from the crossing point, the result in (30) transforms into result (22). We illustrate the result (30) of the modified perturbation theory, which is essentially the correct choice of wave functions for the zeroth-order approximation, in Fig. 4 for the crossing of the unperturbed levels E^{+}_{4} and E^{+}_{7}. As we can see from Fig. 4, expressions (30) smoothly interpolate the results of the standard second-order perturbation theory, Eq. (22), before and after the degeneracy point. Even in the close vicinity of the crossing point, the energies $E_{\pm}$ are different from the eigenvalues $\Lambda_{\pm}$ of the matrix A, i. e., transitions to other levels are important. The energy levels found from Eq. (30) are in good agreement with numerical diagonalization of Hamiltonian (14).

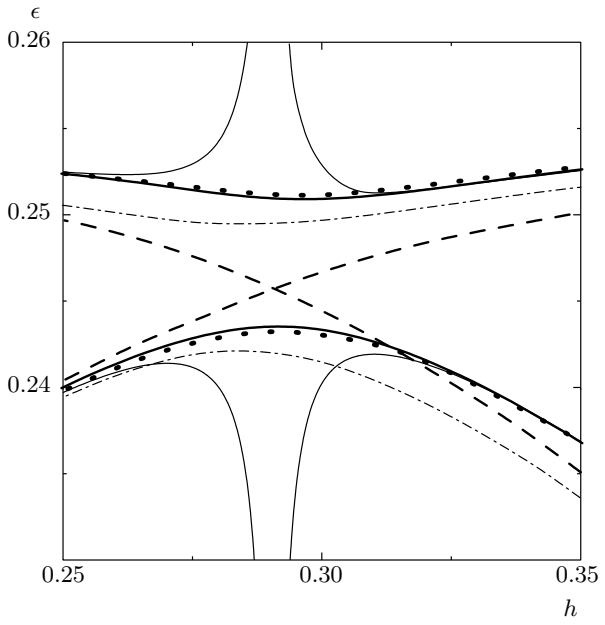

Fig. 4. The dependence of dimensionless unperturbed energies E^{+}_{4}/Δ and E^{+}_{7}/Δ on dimensionless magnetic field $h = 4\pi v^2/(l_H\Delta)^2$ (dashed curves) near their crossing point. The thin solid curves illustrate the results of the standard perturbation theory (see Eq. (22)). The dot-dashed curves are the eigenvalues $\Lambda_{\pm}$. The thick solid black curves are the result of the modified perturbation theory (see Eq. (30)). The points represent the results of numerical diagonalization of the truncated Hamiltonian with 2000 levels. The dimensionless parameter of hexagonal warping is $\alpha = 0.1$ and $g_L = 0$

4. LANDAU LEVELS IN THE WKB APPROXIMATION

To study the structure of Landau levels at higher energies, we use the WKB approach [31]. We employ the Bohr–Sommerfeld quantization condition

$$S(E) = 2\pi l_H^{-2}\big(n + \delta(E)\big), \quad (31)$$

where $S(E)$ denotes the area bounded by a curve of the constant energy E in the momentum space in the absence of the magnetic field, n is an integer number, and $\delta(E)$ contains information on the number of turning points of a semiclassical electron orbit and the Berry phase [32]. Typically, the function $\delta(E)$ is of the order of unity. Since we are interested in Landau levels with $n \gg 1$, we omit $\delta(E)$ below. We also neglect the Zeeman splitting, assuming that the g-factor is not strongly enhanced in comparison with its band value.

The area $S(E)$ can be expressed through the density of states without a magnetic field. As follows from the results in Sec. 2, for some values of ϵ and α there are several disconnected regions enclosed by constant-energy curves. In this case, semiclassical quantization condition (31) has to be applied to each disconnected area separately. For energies in the interval

$$0 < \epsilon < \min\{\epsilon_{+}(\alpha), 1/4\}$$

(see regions *A1* and *A4* in Fig. 1*b*), there is one snowflake-like region including the $\bar{\Gamma}$ point and six outermost regions of infinite area (see Fig. 3). The area of the central region can be written as

$$S_1 = \frac{\Delta^2}{2v^2}\left[2\pi c_1 + 12 \int_{c_1}^{x_1} dx\, \mathcal{G}(x, \epsilon, \alpha) \right], \quad (32)$$

where we introduce the function

$$\mathcal{G}(x,\epsilon,\alpha)=\frac{1}{3}\arccos\frac{-\sqrt{(x+\epsilon)^2-x}}{\sqrt{\alpha x^3}}-\frac{\pi}{6}. \quad (33)$$

It can be shown that

$$\frac{\partial S_1}{\partial\epsilon}=4\pi^2\Delta g_1(\epsilon),\quad g_1(\epsilon)=\frac{\Delta}{2\pi v^2}F_1(\epsilon,\alpha). \quad (34)$$

The function $g_1(\epsilon)$ provides the contribution to the density of states $g(\epsilon)$ from the states in this snowflake-like central region. The area of each among the six outermost regions is

$$S_5=\frac{\Delta^2}{v^2}\int\limits_{x_2}^{\infty}dx\,\mathcal{G}(x,\epsilon,\alpha). \quad (35)$$

Again, this area can be related to the corresponding contribution to the density of states:

$$\frac{\partial S_5}{\partial\epsilon}=\frac{2\pi^2\Delta}{3}g_5(\epsilon),\quad g_5(\epsilon)=\frac{\Delta}{2\pi v^2}F_5(\epsilon,\alpha). \quad (36)$$

Since the integral in Eq. (35) diverges at the upper limit, it is convenient to rewrite Eq. (35) as

$$S_5(\epsilon)=\frac{1}{6}S(0)+\frac{\pi\Delta^2}{3v^2}\int\limits_0^{\epsilon}d\epsilon' F_5(\epsilon',\alpha). \quad (37)$$

Here, $S(0)$ is the total area enclosed by the constant-energy curve $\epsilon=0$. We note that in the framework of Hamiltonian (1), the area $S(0)$ is infinite. It becomes finite, for example, if we take correction to the mass m of the next order in k^2 into account. Within the semiclassical approximation, the Bohr–Sommerfeld quantization condition (31) for $S_5(\epsilon)$ results in sixfold degenerate levels. The quantum tunneling (magnetic breakdown) removes this degeneracy [31].

In the case

$$\max\{0,\epsilon_+(\alpha)\}<\epsilon<1/4$$

(see region *A3* in Fig. 1*b*), there are two disconnected parts of the area (see Fig. 3). The area of the innermost part is given by Eq. (34), whereas the area of the outermost part is

$$S_{2,3}=\frac{6\Delta^2}{v^2}\left(\int\limits_{x_2}^{c_2}dx\,\mathcal{G}(x,\epsilon,\alpha)+\int\limits_{c_3}^{\infty}dx\,\mathcal{G}(x,\epsilon,\alpha)\right)+\\+\frac{\Delta^2}{2v^2}(2\pi c_3-2\pi c_2). \quad (38)$$

Again, we find

$$\frac{\partial S_{2,3}}{\partial\epsilon}=4\pi^2\Delta g_{2,3}(\epsilon),\ g_{2,3}(\epsilon)=\\=\frac{\Delta}{2\pi v^2}\big(F_2(\epsilon,\alpha)+F_3(\epsilon,\alpha)\big). \quad (39)$$

It is convenient to rewrite $S_{2,3}$ as

$$S_{2,3}=S(0)+\frac{2\pi\Delta^2}{v^2}\int\limits_0^{\epsilon}d\epsilon'\Big[F_2(\epsilon',\alpha)+F_3(\epsilon',\alpha)\Big]. \quad (40)$$

In the other case $1/4<\epsilon$ (see Fig. 3), there is always one connected region whose area can be written as

$$S(\epsilon)=S(0)+4\pi^2\Delta\int\limits_0^{\epsilon}d\epsilon' g(\epsilon'). \quad (41)$$

For $\epsilon<0$, the area can be found using the relation

$$\frac{\partial S}{\partial\epsilon}=4\pi^2\Delta\big(g_5(\epsilon)-g_1(\epsilon)\big). \quad (42)$$

The structure of Landau levels undergoes changes near such singularities of the zero-field density of states, which are related to the change of the number of connected parts of the area enclosed by a constant-energy curve.

For $\alpha<\alpha_0$, the sixfold degenerate levels transform into nondegenerate levels at $\epsilon=\epsilon_+(\alpha)$. Using Eq. (11), we can estimate the change in the level spacing at $\epsilon=\epsilon_+(\alpha)$. We find

$$\frac{d\epsilon}{dn}=\frac{h}{4\Delta_+\ln(1/|\epsilon-\epsilon_+|)}\times\\\times\begin{cases}6, & \epsilon_+-\epsilon\ll 1,\\ 1, & \epsilon-\epsilon_+\ll 1,\end{cases} \quad (43)$$

where

$$h=4\pi v^2/(l_H\Delta)^2$$

stands for the dimensionless magnetic field. Thus, the sixfold degenerate levels (corresponding to six disconnected pieces) are six times sparser than the levels after the disconnected pieces merged together. Also, the slope of the sixfold degenerate levels with respect to the magnetic field is six times larger than the slope of levels after consolidation of the disconnected pieces. The levels corresponding to the area S_1 are continuous at $\epsilon=\epsilon_+(\alpha)$. But at $\epsilon=1/4$, the area S_1 merges with the area $S_{2,3}$. Using Eq. (10), we can estimate the level spacing before and after the consolidation:

$$\frac{d\epsilon}{dn}=\frac{h\sqrt{\alpha}}{16\ln(1/|\epsilon-1/4|)}\begin{cases}2, & 1/4-\epsilon\ll 1,\\ 1, & \epsilon-1/4\ll 1.\end{cases} \quad (44)$$

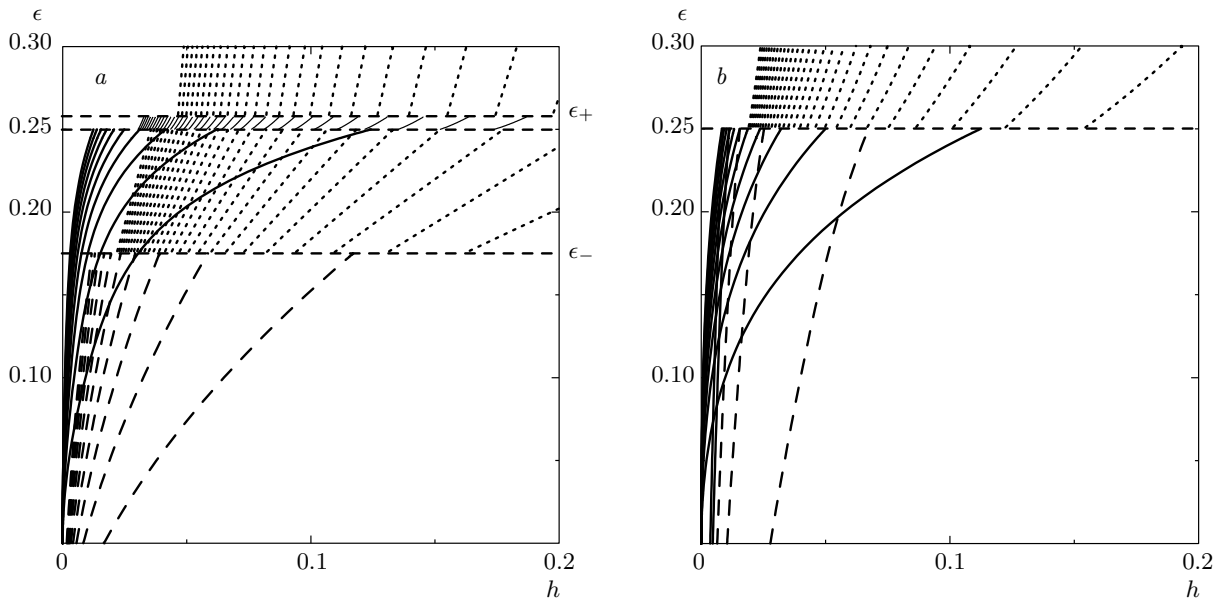

Fig. 5. The structure of Landau levels in the WKB approximation (each 10th level is shown) for $\alpha = 0.4$ (a) and 2 (b). Solid curves denote the levels due to the central snowflake-like area S_1. Dashed curves are sixfold degenerate levels. Dot-dashed curves correspond to levels due to the area obtained after the consolidation of six disconnected outermost pieces. Thin solid curves are the levels corresponding to unified area but with six empty spots. Dotted curves denote the levels in the case where the empty spots disappear. The total area at $\epsilon = 0$ is chosen to be equal to $S(0) = \Delta^2/2v^2$

Each of the Landau levels corresponding to the areas S_1 and $S_{2,3}$ is twice sparser than the levels after consolidation. Also, the slope of these levels at $\epsilon = 1/4$ becomes two times smaller.

For $\alpha > \alpha_0$, Landau levels undergo reconstruction at $\epsilon = 1/4$ only. At $1/4 - \epsilon \ll 1$, there are two sets of levels: the sixfold degenerate ($\epsilon_{2,3}$) and nondegenerate (ϵ_1) ones with the level spacings

$$\begin{aligned} \frac{d\epsilon_1}{dn} &= \frac{h\sqrt{\alpha}}{8\ln[1/(1/4-\epsilon)]}, \\ \frac{d\epsilon_{2,3}}{dn} &= \frac{3h\sqrt{\alpha}}{4\ln[1/(1/4-\epsilon)]}. \end{aligned} \tag{45}$$

The sixfold degenerate levels are six times sparser and steeper than the levels after the disconnected pieces merged together. At $\epsilon > 1/4$, there is only a single set of Landau levels with the spacing

$$\frac{d\epsilon}{dn} = \frac{h\sqrt{\alpha}}{16\ln[1/(\epsilon-1/4)]}. \tag{46}$$

These levels are two times sparser and smoother than ϵ_1 levels.

We illustrate the transformations of Landau levels discussed above in Fig. 5 for two values of the dimensionless parameter of hexagonal warping, $\alpha = 0.4$ and $\alpha = 2$. There are several interesting features due to the hexagonal warping in the structure of the Landau levels. At first, hexagonal warping leads to the existence of sixfold degenerate levels (red curves in Fig. 5) within the WKB approximation for $\epsilon < \min\{\epsilon_+, 1/4\}$. The account of quantum tunneling (magnetic breakdown) should remove this degeneracy. Next, due to the hexagonal warping, there exist levels (green curves in Fig. 5) with energies well above $\Delta/4$, which is not possible in the case $\alpha = 0$. However, it is not clear in the WKB approximation how the Landau levels at $\alpha = 0$ transform to produce levels with energies above $\Delta/4$ in the case $\alpha > 0$. Therefore, we compare the results of the WKB approximation with the Landau levels obtained by numerical diagonalization of Hamiltonian (14) truncated to 2000 levels. As we can see from Fig. 6, the numerical results are in qualitative agreement with the semiclassical treatment.

5. DISCUSSIONS AND CONCLUSIONS

Using recent results of spin and angle resolved photoemission spectroscopy [9], we estimate the parameters relevant for the model considered above for two topological insulators, Bi_2Te_3 and Bi_2Se_3. We note

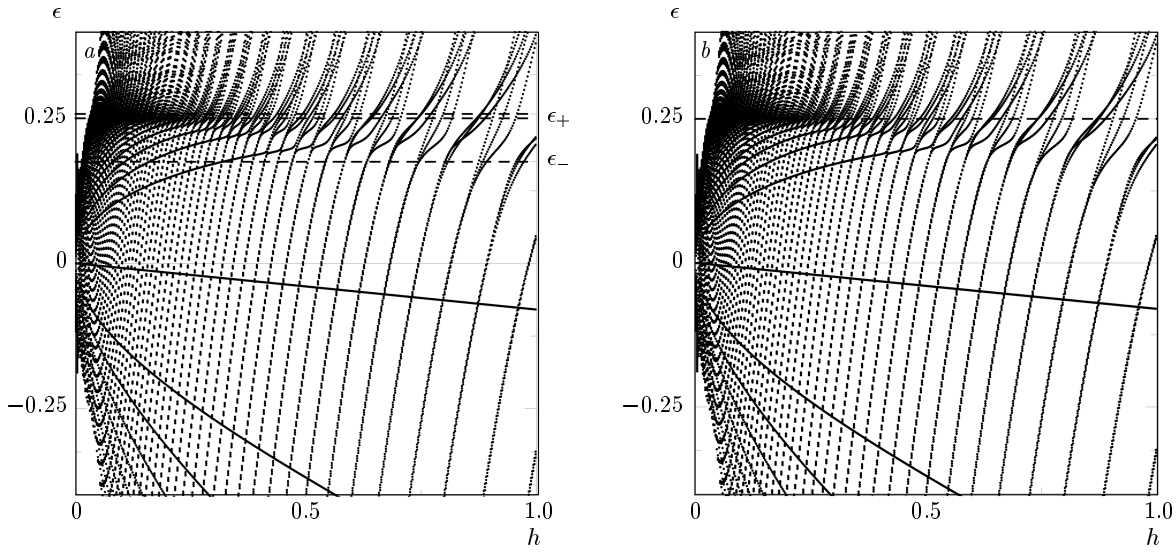

Fig. 6. The structure of Landau levels from numerical diagonalization of the truncated Hamiltonian with 2000 levels for $\alpha = 0.4$ (a) and 2 (b)

Table 2. Estimates for parameters of the model extracted from Ref. [9]

	Δ, eV	E_0, eV	α	k_0, Å^{-1}	h/H, T^{-1}
Bi_2Te_3	1.1	0.51	22	0.14	$2.2 \cdot 10^{-3}$
Bi_2Se_3	0.34	0.43	0.4	0.08	$7.0 \cdot 10^{-3}$

that they differ by the sign of the effective mass m. It is negative for Bi_2Te_3 and positive for Bi_2Se_3. Estimates for parameters of the model extracted from Ref. [9] are summarized in Table 2. We emphasize that although the energy scales Δ and E_0 are of the same order for both topological insulators, the dimensionless parameter α characterizing the strength of the hexagonal warping differs by more than 50 times.

The most interesting theoretical observation is the logarithmic singularity in the TDOSS at $E = \Delta/4$, which corresponds to consolidation of the snowflake-like central region and the six outermost disconnected regions. It occurs in certain directions of the momentum space, e. g., at the angle $\theta = \pi/6$. The condition

$$E_+(k_0, \pi/6) = \Delta/4$$

is solved by the momentum

$$k_0 = \frac{\Delta}{2v}.$$

According to the estimates in Table 2, it is much smaller than the size of the surface Brillouin zone, which is of the order of 1 Å^{-1}. We note that for such a momentum, the ratio of the hexagonal warping term to the term linear in momentum is of the order of

$$\lambda k_0^2/v = \sqrt{\alpha}/4.$$

This indicates that for $\alpha/16 \ll 1$, the singularity occurs in the regime where the hexagonal warping is a small correction to the dispersion linear in k. These estimates are in favor of the use of Hamiltonian (1), which was derived near the $\bar{\Gamma}$ point, for describing the singularity in TDOSS at $E = \Delta/4$.

The spin and angle resolved photoemission spectroscopy for Bi_2Te_3 and Bi_2Se_3 indicates that the energy spectrum of surface states is a monotonic function of momentum above the Dirac point. Therefore, for these materials, the singularities of TDOSS predicted in our work are situated at energies in the bulk conduction band, and are therefore unobservable. Nevertheless, our results provide a theoretical explanation for the typical scanning tunneling microscopy experiments in such materials [15]. If we choose a very large value of the parameter α, then in the energy interval $0 < E < \Delta/4$, the function $F(\epsilon, \alpha)$ has a step-like feature. We present the dependence of $F(\epsilon, \alpha)$ on ϵ in Fig. 7 for $\alpha = 2000$ (this is the minimal value for which the dependence is still step-like). This plot looks much like the experimental one in Ref. [15]. We note that such an enormous increase in the parameter α in comparison with the estimate for Bi_2Te_3 (see Table 2) can be

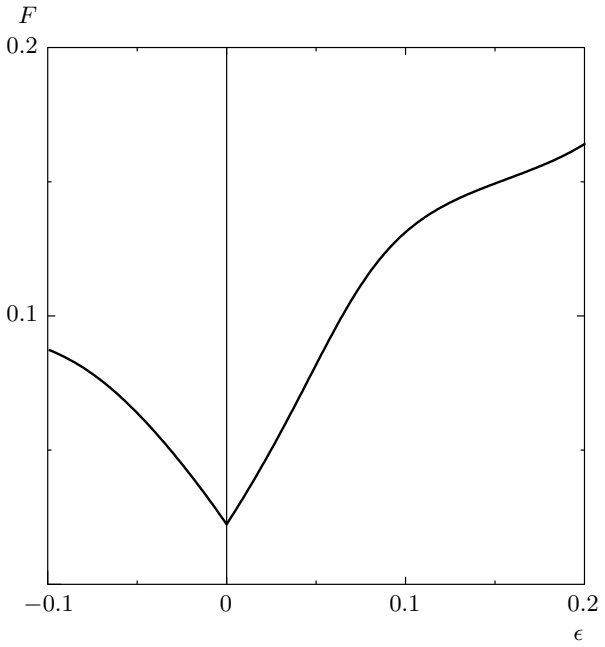

Fig. 7. The dependence of $F(\epsilon, \alpha)$ on ϵ for $\alpha = 2000$

achieved, e. g., by increasing the effective mass by three times.

Finally, we stress the smallness of dimensionless magnetic field h for both Bi_2Te_3 and Bi_2Se_3 (see Table 2). It implies the smallness of the parameter

$$\omega_c l_H/v = \sqrt{h/\pi}.$$

The validity of the perturbation theory for Landau levels with a small level index is controlled by the parameter $\sqrt{\alpha}h/4\pi$. Therefore, for moderate values of α, low-lying Landau levels are not significantly affected by the presence of the finite curvature and hexagonal warping and, hence, scale as $\sqrt{H}$. Such scaling for Landau levels near the Dirac point was recently observed from oscillations in the tunneling conductance of Bi_2Se_3 [18], of Sb_2Te_3 [21], from microwave spectroscopy in Bi_2Te_3 [34], and from magneto-infrared spectroscopy in $Bi_{0.91}Sb_{0.09}$ [35]. The effect of hexagonal warping is most pronounced near the degeneracy points of the unperturbed Landau levels. For a given $h \ll 1$, the degeneracy point corresponds to Landau levels with $n_h \sim \pi/(2h) \gg 1$ and energies of the order of $\Delta/4$. The hexagonal warping leads to avoiding the crossing of Landau levels $E^+_{n_h}$ and $E^+_{n_h+3}$ with the typical distance between them of the order of

$$\delta_h \sim \frac{\sqrt{\alpha/2}\Delta h}{8\pi}.$$

An additional signature of hexagonal warping is the existence of oscillations in the tunneling conductance in the magnetic field at energies above $\Delta/4$. In the case of Bi_2Te_3 for the magnetic field $H = 10$ T, we can estimate $n_h \approx 70$ and $\delta_h \sim 3$ meV. We expect that future tunneling experiments on topological insulators with warped electronic spectra will indeed reveal the predicted complex structure of Landau levels and their unusual evolution in the magnetic field.

To summarize, we computed the tunneling density of surface states $g(E)$ in a 3D topological insulator in the presence of hexagonal warping and finite curvature. We found that hexagonal warping transforms the square-root van Hove singularity of $g(E)$ into a logarithmic one. With an increase in the hexagonal warping, the singularity becomes weaker. For the hexagonal warping values $\lambda \lesssim 0.18/m^2v$, the tunneling density of states has an additional logarithmic singularity and a jump. Their positions and amplitudes depend on λ. In the presence of a perpendicular magnetic field, we analyzed structure of the Landau levels within the perturbation theory in the hexagonal warping and in the WKB approximation. We obtained that hexagonal warping removes degeneracies of the Landau levels and drastically changes their behavior with the magnetic field.

We are grateful to V. Stolyarov, C. Brun, and D. Roditchev for sharing their experimental data [17] prior to publication, which motivated us for the present work. The results in Sec. 2 were obtained within the grant №14.587.21.0006 (RFMEFI58714X0006) of the Ministry of Education and Science of the Russian Federation. The results presented in Secs. 3–4 were obtained with financial support from the Russian Science Foundation under the grant № 14-12-00898.

REFERENCES

1. M. Z. Hasan and C. L. Kane, Rev. Mod. Phys. **82**, 3045 (2010).
2. X.-L. Qi and S.-C. Zhang, Rev. Mod. Phys. **83**, 1057 (2011).
3. Y. Ando, J. Phys. Soc. J. **82**, 102001 (2013).
4. L. Fu, Phys. Rev. Lett. **103**, 266801 (2009).
5. C.-X. Liu, X.-L. Qi, H. J. Zhang, X. Dai, Z. Fang, and S.-C. Zhang, Phys. Rev. B **82**, 045122 (2010).
6. Y. Chen, J. G. Analytis, J.-H. Chu, Z. K. Liu, S.-K. Mo, X. L. Qi, H. J. Zhang, D. H. Lu, X. Dai, Z. Fang, S.-C. Zhang, I. R. Fisher, Z. Hussain, and Z.-X. Shen, Science **325**, 178 (2009).

7. Zh. Alpichshev, J. G. Analytis, J.-H. Chu, I. R. Fisher, and A. Kapitulnik, Phys. Rev. B **84**, 041104 (2011).

8. K. Kuroda, M. Arita, K. Miyamoto, M. Ye, J. Jiang, A. Kimura, E. E. Krasovskii, E. V. Chulkov, H. Iwasawa, T. Okuda, K. Shimada, Y. Ueda, H. Namatame, and M. Taniguchi, Phys. Rev. Lett. **105**, 076802 (2010).

9. M. Nomura, S. Souma, A. Takayama, T. Sato, T. Takahashi, K. Eto, K. Segawa, and Y. Ando, Phys. Rev. B **89**, 045134 (2014).

10. C. M. Wang and F. J. Yu, Phys. Rev. B **84**, 155440 (2011).

11. X. Xiao and W. Wen, Phys. Rev. B **88**, 045442 (2013).

12. S. Smirnov, Phys. Rev. B **88**, 205301 (2013).

13. Z.-G. Fu, F. Zheng, Z. Wang, and P. Zhang, Prog. Theor. Exp. Phys. 103I01 (2013).

14. S. Urazhdin, D. Bilc, S. D. Mahanti, S. H. Tessmer, Th. Kyratsi, and M. G. Kanazidis, Phys. Rev. B **69**, 085313 (2004).

15. Zh. Alpichshev, J. G. Analytis, J.-H. Chu, I. R. Fisher, Y. L. Chen, Z. X. Shen, A. Fang, and A. Kapitulnik, Phys. Rev. Lett. **104**, 016401 (2010).

16. P. Sessi, M. M. Otrokov, T. Bathon, M. G. Vergniory, S. S. Tsirkin, K. A. Kokh, O. E. Tereshchenko, E. V. Chulkov, and M. Bode, Phys. Rev. B **88**, 161407(R) (2013).

17. V. S. Stolyarov, T. Cren, C. Brun, S. I. Bozhko, L. V. Yashina, and D. Roditchev in preparation.

18. T. Hanaguri, K. Igarashi, M. Kawamura, H. Takagi, and T. Sasagawa, Phys. Rev. B **82**, 081305(R) (2010).

19. T. Zhang, N. Levy, J. Ha, Y. Kuk, and J. A. Stroscio, Phys. Rev. B **87**, 115410 (2013).

20. Y.-S. Fu, M. Kawamura, K. Igarashi, H. Takagi, T. Hanaguri, and T. Sasagawa, arxiv:1408.0873 (unpublished).

21. Y. Jiang, Y. Wang, M. Chen, Z. Li, C. Song, K. He, L. Wang, X. Chen, X. Ma, and Q.-K. Xue1, Phys. Rev. Lett. **108**, 016401 (2012).

22. A. Yu. Dmitriev, N. I. Fedotov, V. F. Nasretdinova, and S. V. Zaitsev-Zotov, arxiv:1408.4991 (unpublished).

23. K. Saha, S. Das, K. Sengupta, and D. Sen, Phys. Rev. B **84**, 165439 (2011).

24. P. Schwab and M. Dzierzawa, Phys. Rev. B **85**, 155403 (2012).

25. M. M. Vazifeh and M. Franz, Phys. Rev. B **86**, 045451 (2012).

26. Yu. A. Bychkov and E. I. Rashba, JETP Lett. **39**, 78 (1984); J. Phys. C: Sol. State Phys. **17**, 6039 (1984).

27. P. G. Silvestrov, P. W. Brouwer, and E. G. Mishchenko, Phys. Rev. B **86**, 075302 (2012).

28. F. Zhang, C. L. Kane, and E. J. Mele, Phys. Rev. B **86**, 081303(R) (2012).

29. S. Basak, H. Lin, L. A. Wray, S.-Y. Xu, L. Fu, M. Z. Hasan, and A. Bansil, Phys. Rev. B **84**, 121401(R) (2011).

30. Z. Yang and J. H. Han, Phys. Rev. B **83**, 045415 (2011).

31. for a review, see e. g. I. M. Lifshitz, M. Y. Azbel, and M. I. Kaganov, *Electronic Theory of Metals*, Nauka, Moscow (1971).

32. L. A. Falkovsky, JETP **49**, 609 (1965); A. Yu. Ozerin and L. A. Falkovsky, Phys. Rev. B **85**, 205143 (2012).

33. M. R. Scholz, J. Sánchez-Barriga, J. Braun, D. Marchenko, A. Varykhalov, M. Lindroos, Y. J. Wang, H. Lin, A. Bansil, J. Minár, H. Ebert, A. Volykhov, L. V. Yashina, and O. Rader, Phys. Rev. Lett. **110**, 216801 (2013).

34. A. Wolos, S. Szyszko, A. Drabinska, M. Kaminska, S. G. Strzelecka, A. Hruban, A. Materna, and M. Piersa, Phys. Rev. Lett. **109**, 247604 (2012).

35. A. A. Schafgans, K. W. Post, A. A. Taskin, Y. Ando, X.-Liang Qi, B. C. Chapler, and D. N. Basov, Phys. Rev. B **85**, 195440 (2012).